Multi-response Optimization Of FDM Process Parameters For 3D-printed PLA+ Bone Screw Using PCA-weighted Taguchi-based Grey Relational Analysis

Sugoro Bhakti Sutono[1,2], Cucuk Nur Rosyidi[1*], Pringgo Widyo Laksono[1], and Eko Pujiyanto[1]

[1] Department of Industrial Engineering, Universitas Sebelas Maret, Surakarta, Central Java 57126, Indonesia
[2] Department of Industrial Engineering, Universitas Muria Kudus, Kudus, Central Java 57126, Indonesia
[*] Corresponding author. E-mail: cucuknur@staff.uns.ac.id

Received: Dec. 27, 2025; Accepted: Jul. 02, 2026

Biodegradable, patient-specific bone screw-like prototypes produced by fused deposition modeling (FDM) require careful selection of process parameters to balance mechanical integrity and manufacturing efficiency. This study optimized FDM parameters for improved PLA+ bone screw-like specimens using an integrated Taguchi-grey relational analysis (GRA) framework with principal component analysis (PCA)-derived weighting. Six parameters were investigated using an L25 orthogonal array with triplicate experiments, and the compressive strength (C_S), printing time (P_T), and part weight (P_W) were aggregated into a weighted grey relational grade (GRG). The factor-level optimum (0.06 mm layer height, 0.6 mm wall thickness, 100% infill density, 210 °C nozzle temperature, 50 °C bed temperature, and 30 mm/s printing speed) increased the composite GRG by 3.11% relative to the best experimental trial, achieving $C_S \approx 44.4$ MPa with moderate P_T (≈ 64.5 min) and P_W (≈ 0.554 g). The optimized condition improved C_S by 23.6% while reducing PT by 2.27% and PW by 3.99% relative to the baseline condition. Analysis of variance identified infill density as the dominant contributor to the multi-response performance, followed by layer height and wall thickness. The results demonstrate the effectiveness of the PCA-weighted GRA for transparent multi-objective optimization in FDM. Compressive strength was used as a screening metric; further torsional, pull-out, insertion/removal torque, and fatigue tests are required for fixation-relevant qualification. The optimized parameter set is therefore presented as a local manufacturing optimum for the tested printer-filament-nozzle configuration, not as a generalized implant-design rule.

Keywords: fused deposition modeling, bone screw, multi-response optimization, Taguchi method, grey relational analysis, principal component analysis

http://dx.doi.org/10.6180/jase.202611_34.007

1. Introduction

Additive manufacturing is increasingly used in biomedical device development, and fused deposition modeling (FDM) enables the cost-effective fabrication of patient-specific polymer components with complex geometries. Because FDM is scalable, design-flexible, and compatible with thermoplastic biomaterials, it has been explored for biodegradable medical-device prototypes, including orthopedic screw-like components. The layer-by-layer nature of FDM also allows the fabrication of geometries that are difficult to produce using conventional subtractive methods [1, 2]. For screw-type biomedical prototypes, this capability is particularly relevant because thread geometry, internal structure, and patient-specific dimensional requirements can be adjusted directly during computer-aided design and slicing.

Among biodegradable polymers, polylactic acid (PLA) and its modified variant, PLA+, have been widely studied owing to their biocompatibility, benign degradation behavior, and suitability for temporary implant applications. PLA degrades into non-toxic by-products and can be processed at relatively low temperatures, which supports its use in biomedical research. In principle, resorbable PLA-based devices can reduce the need for secondary removal surgery compared to permanent metallic implants [3, 4]. Accordingly, PLA-based materials have been investigated for orthopedic applications requiring a balance between mechanical integrity and biological compatibility [5–7]. Compared with neat PLA, PLA+ is more practical for FDM studies because commercial formulations are designed to improve toughness and printability while retaining PLA's processing advantages.

Recent studies have also highlighted practical factors that influence the performance and manufacturability of FDM-printed PLA systems. Sterilization and recycling can modify the mechanical and surface properties, raising post-processing and reuse considerations [8]. Reinforcement strategies, including the use of carbon fiber or cellulose nanocrystal additives, can enhance the mechanical performance and introduce multifunctionality [9, 10]. Process-related factors, such as cooling conditions and lubrication, can further affect interlayer bonding and overall part performance [11]. Collectively, these findings emphasize that material formulation, process parameters, and post-processing must be considered together to achieve reliable PLA/PLA+ components. Therefore, optimization studies should evaluate not only strength but also manufacturing efficiency and material consumption.

Neat PLA is inherently brittle, which reduces its reliability under dynamic load-bearing conditions. PLA + formulations, achieved through blending or the use of additives, have been reported to improve ductility and impact resistance [11–14]. Such modifications can alter melt-flow behavior and interlayer diffusion during extrusion, thereby increasing the sensitivity of the final properties to FDM parameters such as layer height, infill density, printing speed, and thermal settings. As a result, material selection and process optimization are strongly coupled with PLA+ components. This coupling is especially important for small screw-like parts, where local bonding quality and internal porosity can strongly influence the effective load path during compression.

For screw-like geometries, a key challenge is to achieve sufficient mechanical integrity while maintaining manufacturing efficiency. Core parameters, such as layer height (LH), infill density (ID), wall thickness (WT), and printing speed (PS), substantially influence the mechanical behavior, printing time, and material consumption (part weight) [15, 16]. Generally, higher infill or thicker walls improve load-bearing capacity but also increase build time and material use [17–19]. Infill density governs the continuity of the internal load path, whereas wall thickness affects the shell-dominated stress distribution in threaded geometries. Conversely, a smaller layer height can improve the surface quality and dimensional fidelity at the cost of longer print times [20, 21]. Layer height can also affect interlayer bonding strength by altering the number of interfaces and the contact area between deposited layers. These effects are material-dependent; for example, PLA and PLA+ can exhibit different sensitivities under similar FDM conditions [14, 18]. Thus, balancing strength, efficiency, and resource utilization is a multi-objective optimization problem.

To address these trade-offs, various optimization approaches have been applied in FDM studies. The Taguchi method (TM) is widely used because orthogonal arrays allow the systematic evaluation of multiple parameters with relatively few experiments [19, 20]. TM has optimized the FDM parameters for PLA parts to improve the tensile strength, dimensional accuracy, and production efficiency [22–24]. For example, previous Taguchi-based studies have shown that process parameters can be screened efficiently in polymer additive manufacturing, but many of these studies evaluate either general PLA specimens or a limited set of performance responses, rather than screw-like biomedical geometries. Combined with analysis of variance (ANOVA), TM also enables a quantitative assessment of factor significance [25, 26]. However, conventional Taguchi optimization is primarily single-response, which limits its applicability to problems with conflicting criteria.

Multi-objective decision frameworks such as grey relational analysis (GRA), TOPSIS, artificial neural networks, and adaptive neuro-fuzzy inference systems have therefore been used to balance mechanical strength, printing time, and material consumption [15, 27, 28]. Grey-based Taguchi methods have been applied to determine trade-offs in FDM-printed orthopedic components [29], including PLA+ structures [30]. Recently, GRA has been integrated with principal component analysis (PCA) to assign data-driven weights to multiple performance characteristics and reduce subjectivity in multi-response ranking [31]. This weighting step is important because equal weighting may not reflect the statistical structure of the experimental responses and can obscure the relative influence of productivity, material use, and mechanical performance. Recent FDM optimization studies further support the use of sta-

Table 1. Concise comparison of representative prior work and the present study

Work/reference	Primary focus	Remaining gap relative to this work	Contribution of the present study
Kechagias [24]	Taguchi-based parameter optimization for 3D printing.	Shows the efficiency of Taguchi design but does not address PLA+ screw-like geometry, biomedical-response framing, or PCA-weighted GRA.	Uses Taguchi design as one component of a validated multi-response framework for PLA+screw-like specimens.
Agarwal et al. [32]	Mechanical behavior of polymer-based orthopedic cortical screws.	Focuses on screw mechanics rather than simultaneous optimization of printing time, part weight, and compressive screening performance.	Links screw-like geometry to manufacturing parameters and experimentally confirms a factor-level optimum.
Kuo et al. [33]	Grey relational analysis for multi-attribute decision-making.	Provides a general GRA method rather than an FDM-specific PLA+ biomedical manufacturing application.	Combines GRA with PCA-derived weights to objectively rank P_T, P_W, and C_s.
Present study	PLA+ bone screw-like specimens fabricated by FDM.	Not applicable.	Integrates L25 Taguchi design, PCA-weighted GRA, ANOVA, and confirmation testing while explicitly limiting claims to manufacturing process optimization.

tistically structured designs and multi-response decision tools for balancing mechanical performance, build time, and material use [23, 24, 31].

Compared with previous studies, the present work differs in scope and integration. Kechagias [24] emphasized the general usefulness of Taguchi design for 3D-printing parameter optimization, Agarwal et al. [32] examined the mechanical behavior of polymer-based orthopedic cortical screws, and Kuo et al. [33] proposed a grey-based Taguchi approach for multi-response decision problems. However, these studies did not jointly address PLA+ material, bone screw-like geometry, the combined responses of printing time, part weight, and compressive strength, and PCA-weighted GRA within one experimentally validated FDM optimization framework.

To make the novelty explicit, Table 1 positions the present study against representative prior work that used Taguchi design, screw-oriented mechanical analysis, or grey-based multi-response decision-making.

Despite these advances, studies employing a combined Taguchi-GRA-PCA framework for PLA+ bone screw-like geometries remain limited, and many focus on tensile behavior rather than compressive performance [32, 33]. For screw-like parts, compression testing provides an initial indicator of structural integrity because the measured strength is strongly influenced by the interlayer bond quality, internal porosity, and effective load-bearing cross-section, all of which are sensitive to FDM parameters. Importantly, this study does not claim that compression alone is sufficient to qualify orthopedic screws for clinical use; torsional strength, pullout resistance, and fatigue durability are also critical for fixation. Accordingly, the compressive strength obtained in this study should not be interpreted as direct evidence of clinical acceptability. ASTM F543 provides screw-specific test methods and performance considerations, but compression testing alone does not establish the suitability of an FDM-printed PLA+ screw-like specimen for orthopedic fixation. Instead, compressive strength is used here as a practical, repeatable screening metric to support manufacturing-focused process optimization and to motivate extending testing to screw-specific functional performance.

To address these gaps, this study integrates TM, GRA, and PCA-based weighting to optimize six key FDM parameters—layer height, wall thickness, infill density, nozzle temperature, bed temperature, and printing speed—for PLA+ bone screw-like specimens. The printing time and part weight were included alongside the compressive strength to capture the trade-offs in productivity and material usage when fabricating screw-like components. The influence factors are quantified using ANOVA, and the underlying physical mechanisms are discussed to aid interpretability for materials- and manufacturing-focused readership. The novelty of this work, therefore, lies in the combined treatment of material selection, screw-like geometry, response selection, and objective PCA-based weighting rather than in any single element alone.

This study was framed as a multi-objective optimization of manufacturing processes for PLA+ bone screw-like components, rather than as an implant qualification study. The main contributions of this study are fourfold: (i) implementation of PCA-derived weighting for multi-objective ranking, with explicit comparison to equal-weight assumptions; (ii) systematic optimization of six FDM parameters for PLA+ bone screw-like specimens using a compact L25 experimental design; (iii) quantitative assessment of factor significance and mechanistic interpretation linking process parameters to interlayer bonding, porosity, and load transfer; and (iv) experimental confirmation of the optimized parameter set, along with a clear statement of limitations and additional testing needed for screw-specific functional qualification.

2. Material and methods

2.1. Material and 3D model

Bone screw-like specimens were manufactured using a commercial PLA+ filament (∅ 1.75 mm; eSUN, Shenzhen, China), a modified PLA designed to improve printability and mechanical performance compared with neat PLA [30]. Prior to printing, the filament was vacuum-dried at 60 °C for 4 h and stored in a desiccator to prevent moisture-induced degradation. The same drying and storage procedure was applied to all experimental runs to reduce moisture-related variability. Key properties from the manufacturer's datasheet are listed in Table 2.

The screw-like prototype geometry was designed with reference to ASTM F543 Type HA specifications [34]. ASTM F543 was used to guide the screw-like geometry and dimensional basis; however, the present experimental protocol was not intended to provide full ASTM F543 mechanical qualification of an orthopedic fixation screw. A SolidWorks CAD model was created and exported as an STL file, then processed in Ultimaker Cura 5.5.0 to set the process parameters, generate G-code, and slice the model for printing. All screw-like specimens were printed on a Creality Ender-6 FDM machine equipped with a 0.2 mm nozzle. Fig. 1 shows the CAD model and key dimensions of the screw.

Table 2. PLA+ filament datasheet properties

Properties	PLA +
Density	1.23 g/cm^3
Extrude temperature	205–225 °C
Bed temperature	60–80 °C
Tensile strength	60 MPa
Flexural strength	74 MPa
Izod impact strength	6 kJ/m^2
Recyclability	Yes

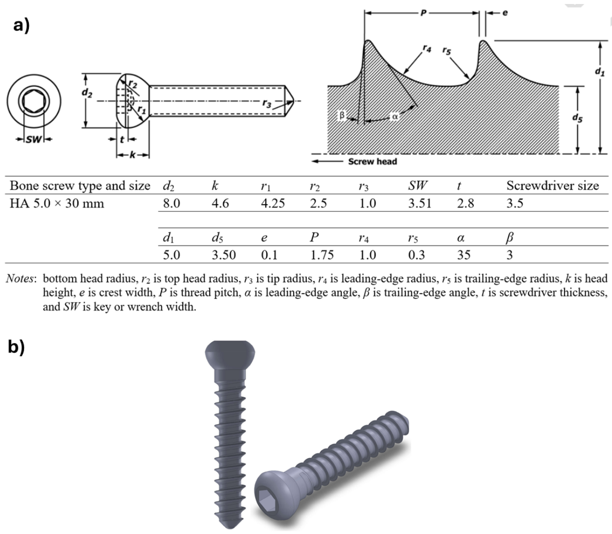

Bone screw type and size	d_2	k	r_1	r_2	r_3	SW	t	Screwdriver size
HA 5.0 × 30 mm	8.0	4.6	4.25	2.5	1.0	3.51	2.8	3.5
	d_1	d_5	e	P	r_4	r_5	α	β
	5.0	3.50	0.1	1.75	1.0	0.3	35	3

Notes: bottom head radius, r_2 is top head radius, r_3 is tip radius, r_4 is leading-edge radius, r_5 is trailing-edge radius, k is head height, e is crest width, P is thread pitch, α is leading-edge angle, β is trailing-edge angle, t is screwdriver thickness, and SW is key or wrench width.

Fig. 1. Bone screw geometry and nominal dimensions.

2.2. Experimental setup and process parameters

The FDM process involves several controllable parameters that significantly influence the printed part's properties. In this study, six process parameters were selected for investigation: layer height (LH), wall thickness (WT), infill density (ID), nozzle temperature (NT), bed temperature (BT), and printing speed (PS). These parameters represent geometric deposition, material volume, thermal, and productivity-related settings that can affect interlayer bonding, internal porosity, load-path continuity, printing time, and part weight. These parameters were selected based on the relevant literature [5, 6, 32, 35–39]. To isolate the effects of the factors, all other printing settings (e.g., build orientation, support strategy, cooling fan, and extrusion flow rate) were held constant across trials. Table 3 lists the six parameters and their levels (ranges) derived from prior studies [5, 6,

Table 3. Process parameters and their corresponding levels.

Process parameters	Symbol	Level 1	Level 2	Level 3	Level 4	Level 5
Layer height (mm)	LH	0.06	0.08	0.10	0.12	0.14
Wall thickness (mm)	WT	0.2	0.4	0.6	0.8	1.0
Infill density (%)	ID	20	40	60	80	100
Nozzle temperature (°C)	NT	195	200	205	210	215
Bed temperature (°C)	BT	40	45	50	55	60
Printing speed (mm/s)	PS	20	30	40	50	60

32]. Fig. 2 outlines the workflow from design and slicing to printing and testing.

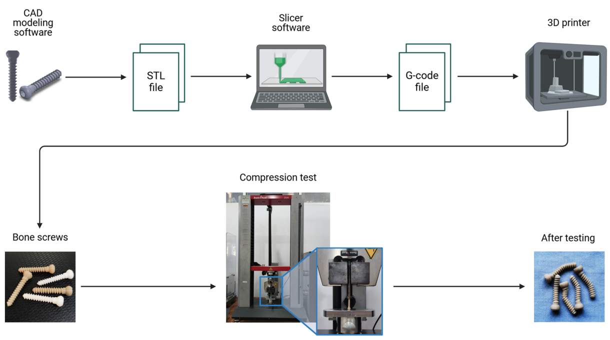

Fig. 2. Schematic of the experimental workflow for design, printing, and testing.

2.3. Design of experiment

A Taguchi experimental design was employed to efficiently study multiple factors while limiting the number of runs. With six parameters at five levels each (Table 3), a full factorial design would require $5^6 = 15,625$ experimental runs. Instead, an L25 (5^6) orthogonal array (OA) was used, consisting of 25 distinct trials. This design was selected to efficiently estimate the main effects of the six process parameters; however, interaction effects were not independently resolved. According to Taguchi's rule, the minimum number of experiments (N_T) can be estimated as

$$N_T = N_P\,(N_L - 1) + 1 \tag{1}$$

where N_P is the number of parameters, and N_L is the number of levels. This yielded $N_T = 25$ for $N_P = 6$ and $N_L = 5$, confirming the choice of the L25 array. The full experimental run matrix is presented in Table 4. Representative printed screw-like specimens produced using various parameter settings are shown in Fig. 3.

2.4. Response variables and measurement

Three response variables were evaluated in this study: printing time (P_T), part weight (P_W), and compressive

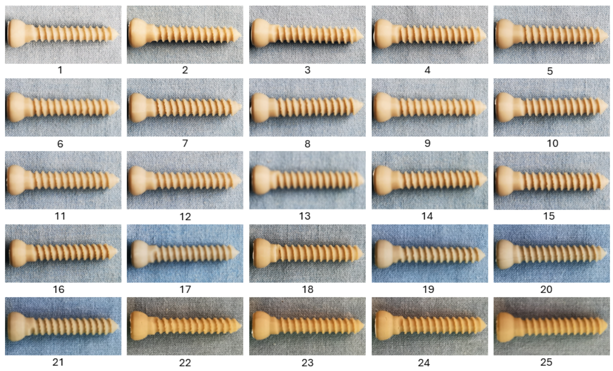

Fig. 3. Samples of PLA+ bone screw-like specimens fabricated using varying process parameters.

strength (C_S). The compressive strength of the printed screw-like specimens was measured using a Zwick/Roell Z020 universal testing machine (20 kN capacity) in accordance with ASTM D695. ASTM D695 was selected to provide a repeatable compressive screening test for the printed screw-like specimens; it was not used as a substitute for screw-specific ASTM F543 tests such as torsion, insertion/removal torque, pull-out, or fatigue evaluation. Compression tests were performed using a 5 kN load cell at a crosshead speed of 1.5 mm/min, and the maximum load before failure was recorded. To ensure uniform axial loading and minimize misalignment, a custom composite fixture was used to hold each screw-like specimen during testing, preventing any slippage. The screw-like specimens were loaded in a platen-to-platen configuration within the fixture, as illustrated in Fig. 2. The printing time for each screw-like specimen was obtained from Ultimaker Cura 5.5.0, which provides a build time estimate during slicing. Therefore, P_T represents slicer-estimated build time rather than direct stopwatch-measured machine time. The weight of each printed screw-like specimen was measured using a high-precision digital balance, calibrated and tared before each measurement. All experiments were conducted in triplicate, and the mean and standard deviation of the three measurements were calculated for each response. The mean values were used for SNR, GRA, PCA, and ANOVA calculations, while the standard deviations were reported to indicate experimental variability.

Measurement uncertainty was treated through replicate-based variability. For C_S and P_W, uncertainty was quantified as the standard deviation of triplicate measurements. For P_T, uncertainty reflects the repeated slicer-estimated build times obtained under the same slicing procedure. Where response plots present experimental mean values, error bars represent ± 1 standard deviation. Taguchi main-effects plots based on SNR level means are presented without replicate-level error bars because they summarize factor-level SNR averages rather than direct specimen-level measurements.

2.5. Multi-objective optimization method

A multi-objective optimization approach was implemented by integrating the Taguchi method, grey relational analysis (GRA), and principal component analysis (PCA) to identify the optimal FDM process parameters for screw-like specimen fabrication. The overall methodology is depicted in Fig. 4. In summary, the process followed these steps: first, a Taguchi L25 design of experiments was performed and signal-to-noise ratios (SNRs) were computed for each response (section 2.5.1). Next, GRA was applied to translate the multi-response problem into a single index: the SNR values were normalized, and grey relational coefficients (GRCs) were calculated for each response, which were then aggregated into a grey relational grade (GRG) for each trial (section 2.5.2). PCA was then used to analyze the GRC correlation matrix and derive objective weights for each response variable; these weights were applied to compute a weighted GRG for each trial (section 2.5.3). An equal-weight GRG was also calculated as a comparison case to evaluate whether PCA-derived weighting changed the ranking outcome. The optimal combination of parameter levels was identified as that yielding the highest GRG (indicating the best overall multi-response performance). Finally, an analysis of variance was conducted to evaluate the effect of each process parameter, and a confirmation experiment was performed to validate the optimized results.

2.5.1. Taguchi method

The Taguchi method was used to compute signal-to-noise ratios (SNRs) for each response to identify factor-level settings robust to experimental variability. For printing time (P_T) and part weight (P_W), the smaller-the-better (STB) criterion was adopted because lower values were desired. For compressive strength (C_S), the larger-the-better (LTB) criterion was adopted to maximize the strength. The SNR values were computed using Eqs. (2) and (3):

$$SNR_{STB} = -10\log_{10}\left[\frac{1}{n}\sum_{i=1}^{n} y_{ij}^2\right] \tag{2}$$

$$SNR_{LTB} = -10\log_{10}\left[\frac{1}{n}\sum_{i=1}^{n} \frac{1}{y_{ij}^2}\right] \tag{3}$$

where y_{ij} is the response for trial i and response j, and n is the number of replicates.

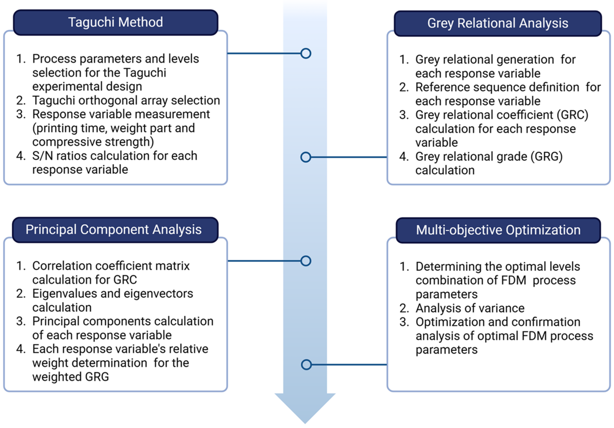

Fig. 4. Multi-objective optimization flowchart.

2.5.2. Grey relational analysis (GRA)

GRA was applied to convert the multi-response problem into a single performance index [33, 40, 41]. Following established GRA procedures [33, 41], this procedure involves four main steps:

1. **Normalization:** STB and LTB formulas (Eqs. (4) and (5)) scaled data between 0 and 1. x_{ij} and y_{ij} denote normalized and raw SNRs, while $\min(y_j)$ and $\max(y_j)$ represent the minimum and maximum SNR values, respectively, observed for response j across all experiments.

$$x_{ij} = \frac{\max\left(y_j\right) - y_{ij}}{\max\left(y_j\right) - \min\left(y_j\right)} \tag{4}$$

$$x_{ij} = \frac{y_{ij} - \min\left(y_j\right)}{\max\left(y_j\right) - \min\left(y_j\right)} \tag{5}$$

2. **Deviation calculation:** deviation $\Delta_{ij} = |x_{0j} - x_{ij}| = |1 - x_{ij}|$ represents distance from ideal.

3. **Grey relational coefficient (GRC):** GRCs (Eq. (6)) measured closeness to the ideal using the distinguishing coefficient $\xi = 0.5$ [42–44].

$$\gamma\left(x_{0j}, x_{ij}\right) = \frac{\Delta_{\min} + \xi\Delta_{\max}}{\Delta_{ij} + \xi\Delta_{\max}} \tag{6}$$

where Δ_{ij} is the deviation of experiment i for response j (as defined above), $\Delta_{\min}$ and $\Delta_{\max}$ are the global minimum and maximum deviation values across all experiments and responses, respectively.

4. **Grey relational grade (GRG):** GRG (Eq. (7)) combined GRCs with PCA-derived weights (from section 2.5.3), providing a single ranking index where higher GRG values meant better performance.

$$\Gamma\left(X_0, X_i\right) = \sum_{j=1}^{n} w_j \cdot \gamma\left(x_0, x_{ij}\right) \tag{7}$$

where w_j is the weight assigned to response j and $\sum_{j=1}^{n} w_j = 1$. A grey relational grade was then obtained for each trial by combining the GRCs of all responses.

2.5.3. *Principal component analysis (PCA)*

PCA was used to determine the objective weights for the responses based on the observed data structure [45, 46]. The GRC values from all trials were compiled, and a correlation matrix was constructed. Eigenvalues (λ_k) and eigenvectors (V_{ik}) of this matrix were obtained by solving the characteristic equation (Eq. (8)).

$$(R - \lambda_k \cdot I_m) \cdot V_{ik} = 0 \tag{8}$$

Larger eigenvalues indicate a higher contribution to the total variance. The first two PCs accounted for approximately 97.8% of the total variance, exceeding the 90% threshold [47]. Therefore, PC1 and PC2 were retained for weight estimation. Each PC is expressed as a linear combination of the original variables:

$$Y_{mk} = \sum_{i=1}^{n} x_m(i).V_{ik} \tag{9}$$

where Y_{m1} represents the first principal component, Y_{m2} represents the second principal component, and so on. Each V_{ik} defines the loading of each variable. The PCA-derived weights were calculated from the squared loadings of P_T, P_W, and C_S in the retained principal components and then normalized so that their sum equaled one. The PCA-derived weights for P_T, P_W, and C_S were used to compute weighted GRGs that provided a data-driven ranking of multi-response performance (see Table 6).

2.6. Statistical analysis

Analysis of variance (ANOVA) was conducted to assess the significance of each process parameter's effect on individual responses and the overall multi-response index. Separate ANOVAs were performed for the SNR of each response (P_T, P_W, C_S) and for the GRG. In each case, the total sum of squares was partitioned among contributions from each factor (and error), and F-tests were conducted at a significance level of $\alpha = 0.05$. A factor with $p < 0.05$ was considered statistically significant for the performance metric.

3. Results and discussion

3.1. The experimental results

Table 4 summarizes the L25 OA design, along with the mean observed values for printing time (P_T), part weight (P_W), and compressive strength (C_S) and their corresponding SNRs. All response values are reported as mean ± standard deviation from three replicate specimens (n = 3), allowing the experimental variability to be traced for each trial. The SNR calculations were performed using Minitab software to ensure consistency with Taguchi definitions.

Substantial variations in performance were observed across the 25 trials. P_T ranged from 23.53 ± 0.20 min (Exp. 22) to 66.00 ± 0.13 min (Exp. 5), reflecting the differences in the number of deposited layers and total extrusion length associated with changes in infill, wall thickness, layer height, and speed. P_W ranged from 0.374 ± 0.002 g (Exp. 1) to 0.605 ± 0.007 g (Exp. 21), consistent with the expected influence of the deposited material volume, which is governed primarily by infill density and wall thickness. The relatively small standard deviations for P_T and P_W indicate that the slicing and weighing procedures were repeatable within the tested conditions.

C_S ranged from 11.518 ± 0.96 MPa (Exp. 1) up to 51.575 ± 1.44 MPa (Exp. 13). The highest strength was observed at 100% infill (Exp. 13) combined with a relatively thicker wall, which increased the load-bearing cross-section and reduced the number of internal voids. This observation agrees with prior findings that higher infill and thicker walls increase the strength by reducing porosity and providing more continuous load paths [48, 49]. Mechanically, a higher infill density improves load-path continuity through the screw core, while a thicker wall increases the shell-supported region that resists compressive stress in the threaded geometry.

The data also demonstrate clear trade-offs among the objectives. For example, Exp. 13 achieved the highest C_S ($\approx$ 51.6 MPa), but also had a relatively high P_W (0.586 g) and a

Table 4. The experimental design using L25 (5^6) orthogonal array, the average experimental results, and SNRs for the responses.

Exp. no.	Process parameters						Printing time		Part weight		Compressive strength	
	LH	WT	ID	NT	BT	PS	Result (min)	SNR (dB)	Result (g)	SNR (dB)	Result (MPa)	SNR (dB)
1	0.06	0.2	20	195	40	20	53.42 ± 0.21	-34.554	0.374 ± 0.002	8.543	11.518 ± 0.96	21.227
2	0.06	0.4	40	200	45	30	59.60 ± 0.17	-35.505	0.472 ± 0.005	6.521	23.581 ± 0.33	27.451
3	0.06	0.6	60	205	50	40	64.58 ± 0.18	-36.202	0.530 ± 0.003	5.514	36.969 ± 1.66	31.357
4	0.06	0.8	80	210	55	50	64.75 ± 0.14	-36.225	0.565 ± 0.002	4.959	37.978 ± 1.87	31.591
5	0.06	1.0	100	215	60	60	66.00 ± 0.13	-36.391	0.577 ± 0.002	4.776	35.919 ± 0.66	31.107
6	0.08	0.2	40	205	55	60	42.93 ± 0.21	-32.656	0.441 ± 0.001	7.111	17.027 ± 0.96	24.623
7	0.08	0.4	60	210	60	20	53.95 ± 0.19	-34.640	0.521 ± 0.002	5.663	30.801 ± 1.36	29.771
8	0.08	0.6	80	215	40	30	53.78 ± 0.20	-34.613	0.569 ± 0.007	4.898	37.613 ± 1.33	31.507
9	0.08	0.8	100	195	45	40	50.75 ± 0.23	-34.109	0.580 ± 0.004	4.731	45.669 ± 1.69	33.192
10	0.08	1.0	20	200	50	50	42.92 ± 0.16	-32.653	0.506 ± 0.005	5.917	24.127 ± 0.38	27.650
11	0.10	0.2	60	215	45	50	38.97 ± 0.14	-31.814	0.503 ± 0.002	5.969	25.510 ± 0.73	28.134
12	0.10	0.4	80	195	50	60	42.60 ± 0.18	-32.588	0.570 ± 0.008	4.883	40.614 ± 0.99	32.174
13	0.10	0.6	100	200	55	20	48.48 ± 0.24	-33.712	0.586 ± 0.003	4.642	51.575 ± 1.44	34.249
14	0.10	0.8	20	205	60	30	33.60 ± 0.11	-30.527	0.465 ± 0.007	6.651	20.270 ± 0.52	26.137
15	0.10	1.0	40	210	40	40	36.67 ± 0.19	-31.285	0.529 ± 0.002	5.531	27.219 ± 0.82	28.697
16	0.12	0.2	80	200	60	40	36.30 ± 0.13	-31.198	0.568 ± 0.009	4.913	38.596 ± 0.77	31.731
17	0.12	0.4	100	205	40	50	37.53 ± 0.15	-31.488	0.596 ± 0.008	4.495	41.720 ± 0.67	32.407
18	0.12	0.6	20	210	45	60	28.45 ± 0.11	-29.082	0.451 ± 0.002	6.916	19.725 ± 0.28	25.900
19	0.12	0.8	40	215	50	20	33.67 ± 0.19	-30.544	0.499 ± 0.005	6.038	22.914 ± 0.59	27.202
20	0.12	1.0	60	195	55	30	33.60 ± 0.20	-30.527	0.548 ± 0.003	5.224	35.637 ± 0.49	31.038
21	0.14	0.2	100	210	50	30	33.90 ± 0.25	-30.604	0.605 ± 0.007	4.365	43.545 ± 0.32	32.779
22	0.14	0.4	20	215	55	40	23.53 ± 0.20	-27.434	0.426 ± 0.002	7.412	12.220 ± 0.20	21.742
23	0.14	0.6	40	195	60	50	27.03 ± 0.21	-28.638	0.495 ± 0.004	6.108	25.102 ± 0.42	27.994
24	0.14	0.8	60	200	40	60	27.20 ± 0.17	-28.691	0.534 ± 0.006	5.449	28.958 ± 1.31	29.235
25	0.14	1.0	80	205	45	20	33.32 ± 0.18	-30.453	0.571 ± 0.003	4.867	32.390 ± 1.27	30.208

long P_T (48.48 min). In contrast, Exp. 22 yielded the shortest P_T (23.53 min), a low P_W (0.426 g), and a much lower C_S ($\approx$ 12.2 MPa). These opposing trends underscore the need for a multi-response optimization framework rather than optimizing each metric independently. Therefore, the best condition cannot be selected solely based on the maximum C_S, minimum P_T, or minimum P_W, because each objective favors a different combination of process parameters.

Before examining the factor effects, the response data were checked for normality. Fig. 5 shows the normal probability plots for P_T, P_W, and C_S. The Anderson-Darling test indicated $p > 0.05$ for all three responses, suggesting no significant deviation from normality at the 5% level. Thus, the use of parametric ANOVA and SNR-based analyses was justified.

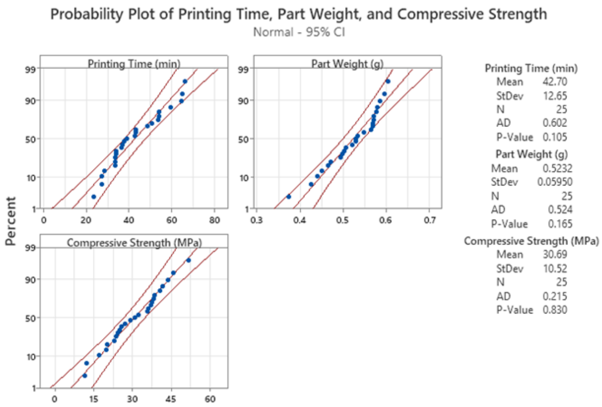

Fig. 5. Normal probability plots of printing time, part weight, and compressive strength.

3.2. Effect of process parameters on response variables

This section analyzes the effect of each FDM parameter on the individual responses—P_T, P_W, and C_S—using the Taguchi SNR results. For each factor, the mean SNR at each level was calculated, and the results are presented in the response table (Table 5) and as main effects plots (Fig. 6). The influence of a given parameter on the response can be gauged by the range Δ of the mean SNR across its levels; a larger Δ indicates a stronger effect.

For FDM-printed PLA+, the statistical effects were in-

Table 5. Response table of SNR for printing time, part weight, and compressive strength.

Response	Process parameters	Symbol	Levels 1	2	3	4	5	Δ	Rank
Printing time	Layer height (mm)	LH	-35.775	-33.734	-31.985	-30.568	-29.164	6.611	1
	Wall thickness (mm)	WT	-32.165	-32.331	-32.449	-32.019	-32.262	0.430	4
	Infill density (%)	ID	-30.850	-31.726	-32.375	-33.015	-33.261	2.411	2
	Nozzle temperature (°C)	NT	-32.083	-32.352	-32.265	-32.367	-32.159	0.284	6
	Bed temperature (°C)	BT	-32.126	-32.192	-32.518	-32.111	-32.279	0.408	5
	Printing speed (mm/s)	PS	-32.780	-32.355	-32.046	-32.164	-31.882	0.899	3
Part weight	Layer height (mm)	LH	6.063	5.664	5.535	5.517	5.640	0.545	3
	Wall thickness (mm)	WT	6.180	5.795	5.616	5.566	5.263	0.917	2
	Infill density (%)	ID	7.088	6.262	5.564	4.904	4.602	2.486	1
	Nozzle temperature (°C)	NT	5.898	5.488	5.728	5.487	5.819	0.411	6
	Bed temperature (°C)	BT	5.783	5.801	5.343	5.870	5.622	0.526	4
	Printing speed (mm/s)	PS	5.951	5.532	5.620	5.490	5.827	0.461	5
Compressive strength	Layer height (mm)	LH	28.546	29.349	29.878	29.656	28.392	1.487	5
	Wall thickness (mm)	WT	27.699	28.709	30.201	29.472	29.740	2.503	2
	Infill density (%)	ID	24.531	27.194	29.907	31.442	32.747	8.215	1
	Nozzle temperature (°C)	NT	29.125	30.063	28.946	29.748	27.938	2.125	3
	Bed temperature (°C)	BT	28.615	28.977	30.232	28.648	29.348	1.618	4
	Printing speed (mm/s)	PS	28.532	29.782	29.344	29.555	28.608	1.251	6

terpreted through coupled process-structure mechanisms rather than as isolated numerical trends. Layer height alters deposited-road overlap and the number of interfacial planes; wall thickness changes the shell-supported load path around the thread; infill density controls core continuity and void content; nozzle temperature governs melt viscosity and interlayer molecular diffusion; and printing speed changes residence time, cooling rate, and road stability. These mechanisms provide the basis for interpreting porosity, stress transfer, and compressive behavior in the following subsections.

3.2.1. *Printing time* (P_T)

The SNR analysis (Table 5, Fig. 6(a)) shows that layer height (LH) is the most influential factor on P_T, with a range $\Delta = 6.611$ dB, followed by infill density (ID) ($\Delta = 2.411$ dB) and printing speed (PS) ($\Delta = 0.899$ dB). The remaining parameters—wall thickness (WT), bed temperature (BT), and nozzle temperature (NT)—exhibited much smaller effects on P_T ($\Delta < 0.5$ dB within the tested range). This ranking indicates that P_T was governed mainly by geometric deposition requirements rather than by thermal settings.

P_T is strongly controlled by LH because it directly determines the number of layers required to build the part. As LH increased from 0.06 mm (Level 1) to 0.14 mm (Level 5), the mean P_T SNR improved from -35.775 dB to -29.164 dB (Table 5), indicating progressively shorter print times with larger layer heights. This monotonic trend (Fig. 6(a)) is expected because increasing LH reduces the total layer count and the associated toolpath length for a given geometry. However, this benefit must be interpreted alongside potential reductions in surface fidelity and interlayer bonding quality at larger layer heights.

ID is the second most important factor for P_T. Increasing the infill from 20% to 100% adds more internal toolpaths and longer extrusion, leading to longer print times (lower P_T SNR). The magnitude of this effect ($\Delta = 2.411$ dB) highlights that print productivity is sensitive to infill level. This result is consistent with the physical role of infill density because increasing the internal material fraction directly increases the amount of deposited filament and the total travel path required to form the screw core.

PS has a measurable but smaller impact: higher speeds generally shorten P_T (higher P_T SNR), with an overall Δ of 0.899 dB across 20–60 mm/s. This relatively modest influence suggests that within this parameter space, changing the deposited volume via LH and ID has a larger effect on P_T than do changes in nominal PS. This may occur because acceleration, deceleration, short toolpaths, and non-printing movements limit how much nominal speed alone reduces total build time for small threaded parts.

WT, NT, and BT had minimal influence on P_T (Δ well below 1 dB). This is reasonable because NT and BT primarily affect layer adhesion and may not significantly alter the required extrusion length, while WT changes the shell thickness, which usually contributes less to the total print time than infill. Thus, within the tested parameter ranges, thermal conditions were more relevant to bonding-related mechanical behavior than to reducing build time.

In summary, to minimize P_T, a larger LH and a lower ID, supplemented by a higher PS (within stable printing limits), should be used. However, because P_T is only one of the objectives, these settings must be balanced against considerations for P_W and C_S in the multiobjective optimization. In particular, the P_T-minimizing condition may reduce compressive performance because low infill can interrupt load-path continuity and large layer height can weaken interlayer bonding.

3.2.2. *Part weight* (P_W)

Based on the SNR results (Table 5, Fig. 6(b)), infill density (ID) was the dominant factor affecting P_W, with $\Delta = 2.486$ dB, followed by wall thickness (WT) ($\Delta = 0.917$ dB) and layer height (LH) ($\Delta = 0.545$ dB). The other parameters—bed temperature (BT), printing speed (PS), and nozzle temperature (NT)—had comparatively minor effects on P_W ($\Delta < 0.53$ dB each within the tested range). This ranking confirms that P_W was controlled primarily by parameters that directly affect the deposited material volume, rather than by thermal or speed-related parameters.

P_W was largely governed by the volume of the material in the part. As expected, increasing ID from 20% to 100% substantially increased P_W: the mean P_W SNR decreased from 7.088 dB at 20% infill to 4.602 dB at 100% infill (Table 5), indicating heavier parts at higher infill densities.

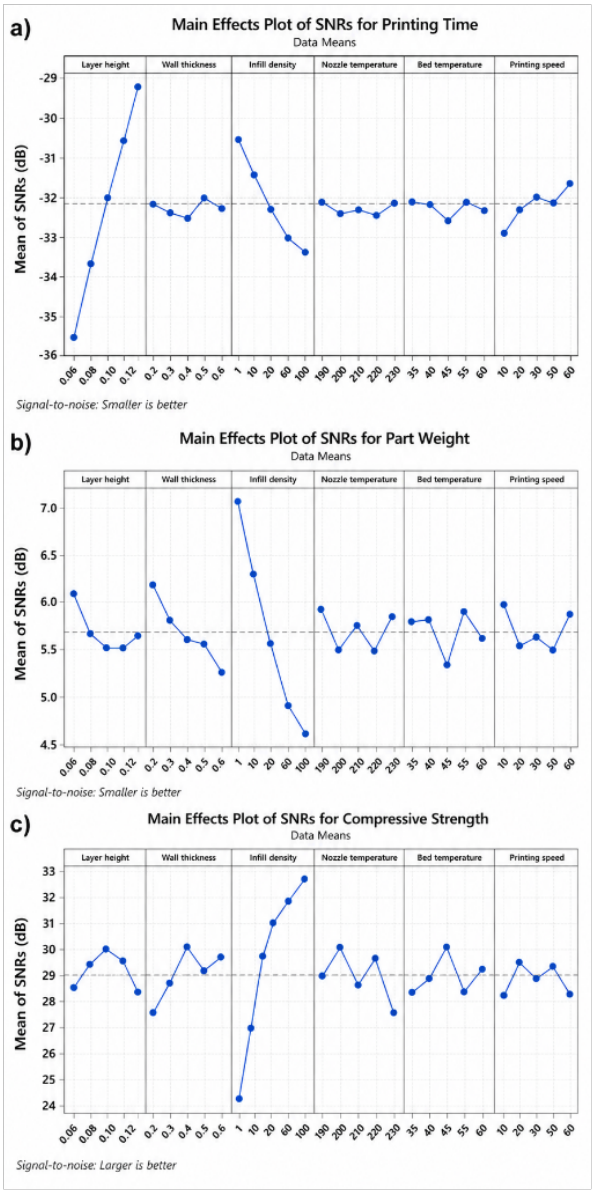

Fig. 6. Main effects plots of SNR for (a) printing time, (b) part weight, and (c) compressive strength.

A higher infill means more plastic is deposited inside the screw, directly raising its mass. Although this increases material consumption, the same increase in internal material can also improve load-path continuity under compression, which explains why P_W and C_S must be optimized together rather than independently.

WT was the second-ranked factor for P_W. Thicker walls add material around the screw periphery, so increasing WT from 0.2 mm (Level 1) to 1.0 mm (Level 5) reduced the mean P_W SNR from 6.180 dB to 5.263 dB. This confirms that thicker shells yield heavier parts. For threaded screw-like geometries, this added shell material is mechanically significant because the outer wall influences stress distribution around the thread and increases the effective load-bearing region.

LH had a smaller influence on weight. Over the range 0.06–0.14 mm, the mean P_W SNR changed only by 0.545 dB . Because the overall part volume is fixed by the geometry, LH does not significantly change the weight; the slight differences observed could arise from differences in its effects on extrusion efficiency and raster overlap during slicing. Nonetheless, LH was a tertiary factor for P_W compared to ID and WT. This result indicates that LH affects PW indirectly via slicing and deposition behavior rather than directly through a change in nominal screw volume.

NT, BT, and PS produced only minor variations in P_W. Any small differences are likely due to subtle changes in extrusion consistency or line bonding, rather than intentional changes in part geometry or volume. Thus, these parameters should be selected primarily based on print stability and mechanical performance rather than on weight reduction.

In summary, P_W was minimized primarily through low ID and thin walls. The other parameters (LH, NT, BT, and PS) can be adjusted based on other considerations (such as mechanical strength or print stability) because their impact on P_W is minimal. However, the lowest-weight condition is not necessarily the most suitable condition for screw-like components, because low ID may interrupt the internal load path and thin walls may reduce the shell contribution to compressive stress resistance.

3.2.3. Compressive strength (C_S)

For compressive strength, the SNR analysis with the larger-the-better criterion (Table 5, Fig. 6(c)) indicates that infill density (ID) is the most influential factor ($\Delta = 8.215$ dB), followed by wall thickness (WT) ($\Delta = 2.503$ dB) and nozzle temperature (NT) ($\Delta = 2.125$ dB). The remaining factors—bed temperature (BT), layer height (LH), and printing speed (PS)—had smaller but non-negligible effects on C_S. This ranking shows that C_S was governed mainly by material distribution and bonding-related factors: ID and WT control the effective load-bearing structure, whereas NT influences interlayer fusion.

The strong effect of ID reflects the critical role of internal porosity and load-bearing area during compression. Raising the infill from 20% to 100% increased the mean C_S SNR from 24.531 dB to 32.747 dB (Table 5), correlating with a major improvement in actual compressive strength (e.g., low-infill samples like Exp. 22 had much lower C_S, whereas high-infill samples like Exp. 9 and Exp. 13 had much higher C_S). A higher infill provides more continuous material to carry the load and fewer voids that can act as stress concentrators.

Therefore, ID improves C_S not only by increasing the amount of material but also by enhancing load-path continuity through the screw core and reducing local stress concentration around internal voids.

The second key factor is the WT. A thicker wall increases the outer load-bearing cross-section of the screw (particularly important for threaded, shell-dominated structures). Accordingly, C_S SNR increased from 27.699 dB at the thinnest wall (WT_1) to 29.740 dB at the thickest wall (WT_5), indicating a meaningful strength gain with thicker shells. In screw-like specimens, the wall region is important because compressive stress is transferred through the outer shell and thread-adjacent material; increasing WT can therefore reduce stress concentration in the peripheral region and improve load sharing between the shell and the infill.

NT also affects C_S, likely due to its influence on interlayer bonding. The main effects plot (Fig. 6(c)) suggests an optimal nozzle temperature at the middle-to-high levels (NT2–NT4), with a slight drop at the highest level. This non-monotonic behavior is plausible because a temperature that is too low can result in poor interlayer fusion, while one that is too high can lead to polymer degradation or excessive melt, weakening the structure. Within the tested 195–215 °C range, the data indicated an optimum near 210 °C. This interpretation is consistent with FDM bonding mechanics, in which adequate melt temperature promotes interdiffusion between adjacent roads and layers, whereas excessive temperature can reduce dimensional stability or degrade the polymer.

BT had a moderate effect on $C_S (\Delta = 1.618$ dB), with the strongest C_S at an intermediate bed temperature (50 °C, Level 3). A warmer bed temperature can improve layer adhesion at the base and reduce thermal stresses, potentially enhancing overall structural integrity, but beyond an optimal point, additional bed heat yields diminishing returns. For small screw-like specimens, excessive bed temperature may also provide little additional benefit, as most compressive load transfer occurs through the deposited screw body rather than solely through the first layers.

LH had a smaller impact on C_S ($\Delta = 1.487$ dB). Extremely thick layers can reduce the interlayer contact area and bonding, while extremely thin layers introduce many interfaces. In this study, a mid-range LH (~ 0.10 mm, Level 3) yielded the highest C_S, suggesting that very low or very high LH is suboptimal for C_S. This result indicates that layer height influences C_S through the balance between interlayer bonding area, number of interfaces, and void formation. Excessively large LH may weaken interlayer adhesion, whereas excessively small LH may increase the number of potential interfacial planes.

PS was the least influential factor for C_S ($\Delta = 1.251$ dB). Variations in print speed between 20 and 60 mm/s had only minor effects on C_S, indicating that within this range, factors controlling material distribution (ID, WT) and bonding (NT, BT) dominate over the slight differences in cooling or deposition quality that speed may impart. Thus, speed-related changes in cooling time and road deposition quality were secondary compared with the structural effects of ID and WT.

Although this study did not include a separate fractographic or microscopic failure-mode analysis, the C_S trends suggest that failure in low-infill specimens is likely promoted by internal voids and discontinuous load paths, whereas higher infill and thicker wall specimens provide more continuous material to resist axial compression. In FDM-printed PLA-based parts, possible compression-related failure mechanisms include brittle cracking, interlayer delamination, local buckling, or combined cracking and delamination, depending on bonding quality, porosity, and geometry. Therefore, future work should include post-failure imaging or fractography to directly verify the dominant failure mode.

In summary, CS was maximized with a high ID and thick walls, along with an optimized NT (around 210 °C), a moderate BT (around 50 °C), and a mid-level LH. Since these parameter choices (high ID, high WT, etc.) tend to increase P_W and P_T, the results reinforce the importance of multi-objective optimization to find a balanced setting. The achieved C_S values should be interpreted as compression-screening results rather than proof of clinical acceptability for cortical bone screws. ASTM F543 emphasizes screw-specific mechanical evaluations, and additional torsional, pull-out, insertion/removal torque, and fatigue tests are required before the printed PLA+ screw-like specimens can be assessed for fixation performance.

3.3. Multi-objective optimization

The single-response Taguchi optimizations for P_T, P_W, and C_S suggested different optimal parameter combinations, confirming the presence of conflicting objectives. From the SNR level means in Table 5, the estimated optimal settings would be: (i) minimum P_T: LH_5–WT_4–ID_1–NT_1–BT_4–PS_5; (ii) minimum P_W: LH_1–WT_1–ID_1–NT_1–BT_4–PS_1; and (iii) maximum C_S: LH_3–WT_3–ID_5–NT_2–BT_3–PS_2. These three sets of conditions are mutually inconsistent. For instance, minimizing P_T and P_W calls for low infill and thinner walls, whereas maximizing C_S requires high infill and thicker walls. This conflict necessitates a multi-objective optimization approach. This result also confirms that the optimum cannot be selected by considering only one performance criterion, because the parameter levels that improve productivity and material economy may reduce compressive performance.

Compared with previous Taguchi-based FDM optimization studies, the present approach combines four elements within a single framework: PLA+ material, bone screw-like geometry, simultaneous evaluation of P_T, P_W, and C_S, and PCA-derived objective weighting. Kechagias [24] demonstrated the usefulness of Taguchi design for 3D-printing parameter optimization, Agarwal et al. [32] investigated the mechanical behavior of polymer-based orthopedic cortical screws, and Kuo et al. [33] established a grey-based Taguchi method for multi-response decision-making. However, these studies did not jointly integrate PLA+ screw-like specimens, manufacturing-efficiency responses, compressive-screening performance, and PCA-weighted GRA with confirmation testing.

To address these trade-offs, Taguchi-based GRA was performed with PCA-derived weights (rather than assuming equal weights for responses). In brief, the SNR values for P_T, P_W, and C_S in Table 4 were first normalized to the range [0,1] using Eqs. (4) and (5), treating P_T and P_W as STB responses and C_S as an LTB response. The deviation of each normalized value from the ideal (1) was calculated, and GRCs were obtained using Eq. (6) with $\xi = 0.5$. These GRCs were then combined to produce an overall GRG for each experiment using Eq. (7). The use of PCA-derived weights was intended to reduce subjectivity in assigning importance to responses and to reflect the variance structure of the experimental GRC data.

Since this analysis uses SNR values (rather than raw measurements), normalization effectively makes the responses dimensionless and comparable. For the STB metrics (P_T and P_W), a lower original value yielded a higher normalized score, while for the LTB metric (C_S), a higher original value yielded a higher normalized score. Under this scheme, a normalized value of 1 indicates the best observed performance for that response, and 0 indicates the worst.

Next, PCA was applied to the GRC matrix. Table 6 shows the PCA results: the first two principal components (PC1 and PC2) account for 97.8% of the variance in the GRC data and were therefore retained. The squared loadings of each response on PC1 and PC2 were summed and normalized to determine weights [31, 45]. The resulting weights were $w_{P_T} = 0.403$, $w_{P_W} = 0.322$, and $w_{C_S} = 0.274$. These reflect the relative contribution of each response to the overall variance in performance. For transparency, an equal-weight case ($w_{P_T} = w_{P_W} = w_{C_S} = 1/3$) was also evaluated to determine whether the choice of weighting would change the outcome. This comparison was included to show whether the proposed PCA weighting changed the selected optimum relative to the common equal-weight assumption.

Table 6. Eigenanalysis of the GRC matrix used for PCA-based weighting.

Component	PC1	PC2	PC3	w_j
Eigenvalue	0.062	0.035	0.002	
Proportion	0.624	0.354	0.022	
Cumulative	0.624	0.978	1	
Cumulative percentage (%)	62.4	97.8	100	
Eigenvectors:				
P_T	0.396	-0.915	0.071	0.403
P_W	0.663	0.339	0.668	0.322
C_s	0.635	0.217	-0.741	0.274

Note: Eigenvalues and variance proportions correspond to principal components, PC1–PC3. Eigenvector entries show the coefficients for each original variable (P_T, P_W, C_S) in the principal components, and the last column gives the squared coefficient (contribution) of each variable in PC1+PC2 (for P_T, P_W, and C_S, respectively), which were used as weights w_j.

Table 7 presents the GRA computations for all trials, including normalized SNR values, deviation sequences, GRCs, GRGs calculated with equal weights, GRGs with PCA weights, and the resulting rank for each trial. The highest GRG value indicates the best overall compromise among the three objectives. The PCA-weighted columns report the weighted contribution of each response to the final GRG, allowing the effect of the weighting scheme to be traced explicitly.

The ranking indicates that Exp. 5 achieved the highest GRG (0.8572), followed by Exp. 4 (0.8342) and Exp. 13 (0.8109). Importantly, these top-ranked trials do not represent the "best" condition for any single response, but rather a compromise that yields simultaneously high normalized performance across P_T, P_W, and C_S according to the PCA-derived weights. For instance, Exp. 13 produced the highest C_S, but its longer PT and higher PW reduced its overall multi-response ranking compared with Exp. 5.

Because P_T and P_W were weighted slightly higher than C_S (Table 6), the ranking favors conditions that maintain acceptable productivity and material economy while still delivering strong compressive performance. This makes the GRG ranking consistent with the stated manufacturing scope. However, this weighting should not be interpreted as a clinical priority ranking; it reflects the statistical variance structure of the present manufacturing dataset.

To derive a factor-level optimum (which may not be present among the 25 trials), Taguchi level-mean analysis was applied to the GRG values. Table 8 reports the mean GRG at each level of each factor, along with Δ (range across levels) and rank. This procedure estimates the best factor-level combination based on the average GRG response of each level rather than simply selecting the best individual experimental run.

Based on Table 8 and Fig. 7, the optimal multi-objective parameter set was determined by selecting the level associated with the highest mean GRG for each control factor. This procedure yielded the combination LH_1–WT_3–ID_5–NT_4–BT_3–PS_2, corresponding to a layer height of 0.06 mm, wall thickness of 0.6 mm, infill density of 100%, nozzle temperature of 210 °C, bed temperature of 50 °C, and printing speed of 30 mm/s. As this setting is derived from factor-level mean responses rather than an individual experiment, it does not necessarily coincide with any single run in the L25 OA; confirmation experiments are therefore required to validate the predicted improvement.

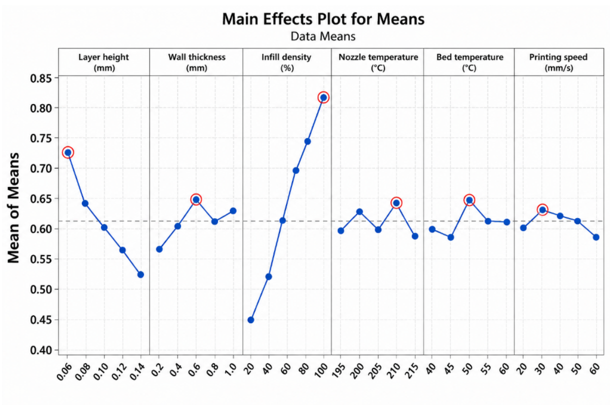

Fig. 7. Graphical representation of the mean PCA-weighted GRG for each process parameter level.

The response range analysis in Table 8 identifies infill density as the dominant parameter influencing the over-

Table 7. Calculated results of the GRA for each experiment, including equal-weight and PCA-weighted GRG rankings.

Exp. no.	Normalization			Deviation sequence			Equal weighting					PCA weighting				
							GRC			GRG	Rank	GRC			GRG	Rank
	P_T	P_W	C_S	P_T	P_W	C_s	P_T	P_W	C_s			P_T	P_W	C_s		
w_j							0.333	0.333	0.333			0.403	0.322	0.274		
1	0.795	0.000	0.000	0.205	1.000	1.000	0.709	0.333	0.333	0.4586	22	0.286	0.107	0.091	0.4846	20
2	0.901	0.484	0.478	0.099	0.516	0.522	0.835	0.492	0.489	0.6054	13	0.337	0.158	0.134	0.6292	12
3	0.979	0.725	0.778	0.021	0.275	0.222	0.960	0.645	0.692	0.7657	5	0.387	0.208	0.190	0.7845	4
4	0.981	0.858	0.796	0.019	0.142	0.204	0.964	0.779	0.710	0.8176	3	0.389	0.251	0.195	0.8342	2
5	1.000	0.901	0.759	0.000	0.099	0.241	1.000	0.835	0.674	0.8366	1	0.403	0.269	0.185	0.8572	1
6	0.583	0.343	0.261	0.417	0.657	0.739	0.545	0.432	0.403	0.4603	21	0.220	0.139	0.111	0.4696	21
7	0.805	0.689	0.656	0.195	0.311	0.344	0.719	0.617	0.593	0.6427	11	0.290	0.199	0.163	0.6509	10
8	0.802	0.872	0.789	0.198	0.128	0.211	0.716	0.797	0.704	0.7387	7	0.289	0.257	0.193	0.7382	6
9	0.745	0.912	0.919	0.255	0.088	0.081	0.662	0.851	0.860	0.7912	4	0.267	0.274	0.236	0.7770	5
10	0.583	0.628	0.493	0.417	0.372	0.507	0.545	0.574	0.497	0.5385	16	0.220	0.185	0.136	0.5407	16
11	0.489	0.616	0.530	0.511	0.384	0.470	0.495	0.566	0.516	0.5253	18	0.199	0.182	0.141	0.5230	17
12	0.575	0.876	0.841	0.425	0.124	0.159	0.541	0.801	0.758	0.7002	9	0.218	0.258	0.208	0.6841	9
13	0.701	0.934	1.000	0.299	0.066	0.000	0.626	0.883	1.000	0.8362	2	0.252	0.284	0.274	0.8109	3
14	0.345	0.453	0.377	0.655	0.547	0.623	0.433	0.477	0.445	0.4519	23	0.175	0.154	0.122	0.4505	23
15	0.430	0.721	0.574	0.570	0.279	0.426	0.467	0.642	0.540	0.5496	15	0.188	0.207	0.148	0.5431	15
16	0.420	0.869	0.807	0.580	0.131	0.193	0.463	0.792	0.721	0.6588	10	0.187	0.255	0.198	0.6396	11
17	0.453	0.969	0.859	0.547	0.031	0.141	0.477	0.941	0.779	0.7327	8	0.192	0.303	0.214	0.7094	8
18	0.184	0.389	0.359	0.816	0.611	0.641	0.380	0.450	0.438	0.4227	24	0.153	0.145	0.120	0.4183	24
19	0.347	0.600	0.459	0.653	0.400	0.541	0.434	0.555	0.480	0.4897	19	0.175	0.179	0.132	0.4854	19
20	0.345	0.794	0.753	0.655	0.206	0.247	0.433	0.708	0.670	0.6037	14	0.175	0.228	0.184	0.5864	14
21	0.354	1.000	0.887	0.646	0.000	0.113	0.436	1.000	0.816	0.7507	6	0.176	0.322	0.224	0.7217	7
22	0.000	0.271	0.039	1.000	0.729	0.961	0.333	0.407	0.342	0.3608	25	0.134	0.131	0.094	0.3593	25
23	0.134	0.583	0.520	0.866	0.417	0.480	0.366	0.545	0.510	0.4738	20	0.148	0.176	0.140	0.4631	22
24	0.140	0.740	0.615	0.860	0.260	0.385	0.368	0.658	0.565	0.5303	17	0.148	0.212	0.155	0.5152	18
25	0.337	0.880	0.456	0.663	0.120	0.310	0.430	0.806	0.617	0.6177	12	0.173	0.260	0.169	0.6022	13

Table 8. Response table for mean PCA-weighted GRG.

Process Parameters	Symbol	Level 1	Level 2	Level 3	Level 4	Level 5	Δ	Rank	Optimal condition
Layer height (mm)	LH	0.718*	0.635	0.602	0.568	0.532	0.186	2	LH_1
Wall thickness (mm)	WT	0.568	0.607	0.643*	0.612	0.626	0.075	3	WT_3
Infill density (%)	ID	0.451	0.518	0.612	0.697	0.775*	0.325	1	ID_5
Nozzle temperature (°C)	NT	0.599	0.627	0.603	0.634*	0.593	0.041	5	NT_4
Bed temperature (°C)	BT	0.598	0.590	0.643*	0.612	0.612	0.053	4	BT_3
Printing speed (mm/s)	PS	0.607	0.625*	0.621	0.614	0.589	0.036	6	PS_2

Note: An asterisk (*) indicates the highest mean GRG at that factor. The optimal condition for each factor is the level with * in the table.

all multi-response performance ($\Delta = 0.325$; Rank 1), followed by layer height ($\Delta = 0.186$; Rank 2) and wall thickness ($\Delta = 0.075$; Rank 3). This ranking is consistent with the mechanics of material extrusion. Infill density and wall thickness directly control the deposited material volume and internal porosity, thereby governing compressive strength (C_S) and affecting printing time (P_T) and part weight (P_W). Layer height primarily determines the number of deposited layers, thereby strongly influencing P_T, and affects interlayer bonding and void morphology. Specifically, higher infill density improves internal load-path continuity, wall thickness modifies shell-supported stress distribution around the thread region, and layer height influences the number and quality of interlayer interfaces.

Mechanistically, increasing infill density and wall thickness enlarges the effective load-bearing cross-section and reduces void-induced stress concentrations, thereby increasing compressive strength. These changes, however, increase part weight and may extend printing time. Conversely, reducing layer height increases the number of layers, typically prolonging printing time but potentially improving the geometric fidelity and interlayer bonding. The selected optimal combination reflects a balanced trade-off among these competing effects: a high infill density is adopted to avoid the substantial loss in compressive strength associated with a low infill, wall thickness is maintained at an intermediate level rather than its maximum, and printing speed, bed temperature, and nozzle temperature are chosen to ensure stable bonding with acceptable productivity. Thus, the optimum does not simply maximize material deposition; instead, it balances a fully filled core with an intermediate wall thickness and moderate thermal-deposition conditions.

To assess the robustness of the optimization, an equal-weight GRA was conducted, assigning identical weights to all responses ($w_j = 1/3$), and compared with the PCA-weighted approach. As shown in Table 7, the equal-weight GRA ranks Exp. 5 as the top trial, with a GRG of 0.8366. The PCA-weighted GRA ($w_{PT} = 0.403$, $w_{PW} = 0.322$, and $w_{CS} = 0.274$) yielded the same optimal experiment, with a higher GRG of 0.8572. The approximately 2.4% increase in GRG indicates that data-driven weighting refines the degree of optimality without altering the experimental ranking. The unchanged top-ranked trial under both weighting schemes supports the robustness of the selected experimental optimum, while the PCAweighted value provides a dataset-specific ranking index.

Finally, within the scope of this study, the optimized parameter set should be interpreted as a manufacturing-oriented compromise for PLA+ bone screw-like specimens subjected to compressive loading. Additional component-specific qualifications, including torsional, pull-out, and fatigue testing, are required before extrapolating these results to orthopedic fixation performance. Therefore, the optimized GRG and the improvement in compressive strength do not, by themselves, demonstrate clinical acceptability. ASTM F543-related screw performance requires additional screw-specific mechanical tests, including torsional behavior, insertion/removal torque, pull-out resistance, and fatigue durability.

3.4. Statistical analysis

ANOVA was performed on GRG to quantify the statistical influence of each process parameter on overall multi-objective performance. For completeness, Table 9 also reports ANOVA results for the individual responses—printing time (P_T), part weight (P_W), and compressive strength (C_S)—which support and contextualize the response-specific trends discussed in section 3.2.

For printing time, layer height was the dominant factor ($p = 0.001$), explaining 84.82% of the total variance owing to its direct control over the layer count and toolpath length. Infill density was the second most influential parameter ($p = 0.001$, 11.80%), while printing speed was statistically significant ($p = 0.004$) but contributed only marginally (1.25%). The other parameters did not have a significant effect on PT within the range investigated.

Part weight was primarily governed by infill density ($p = 0.001$), which accounts for 76.67% of the variance by directly controlling the volume of deposited internal material. Wall thickness also showed a statistically significant but smaller contribution ($p = 0.003$, 8.14%), reflecting the effect of increased shell material. No other factors significantly affected PW.

Compressive strength was also dominated by infill density ($p = 0.001$; 77.33%), consistent with the reduced porosity and increased effective load-bearing area at higher infill levels. Wall thickness had a modest but statistically significant effect ($p = 0.047$, 4.25%). In contrast, layer height was not significant for C_S ($p = 0.999$), indicating that its influence was indistinguishable from the experimental scatter under the tested compressive loading conditions. Nozzle temperature, bed temperature, and printing speed were also not significant for C_S at $\alpha = 0.05$. These results support the mechanical interpretation that load-path continuity and shell-supported stress distribution were more influential than layer height variation in determining compressive strength within the tested range.

For the composite GRG, infill density and layer height were highly significant ($p < 0.05$) and together explained most of the observed variation, contributing 71.69% and 20.00%, respectively, while the residual error accounted for 6.26%. Wall thickness showed a marginal but statistically significant effect ($p = 0.049$, 1.55%), whereas nozzle temperature, bed temperature, and printing speed were not significant, each contributing $\leq 0.26\%$. Overall, these results confirm that infill density and layer height are the primary levers for multi-objective optimization, with wall thickness contributing secondarily. The dominance of infill density in GRG is expected because this factor simultaneously affects C_S, P_W, and P_T, whereas layer height mainly influences P_T and interlayer morphology.

3.5. Confirmation test

To validate the factor-level optimum identified using the TM–GRA–PCA framework, confirmation experiments were conducted by fabricating and testing PLA+ bone screw-like specimens at the optimized parameter combination. The resulting performance was benchmarked against a baseline condition defined as the best-performing experiment within the original L25 OA, corresponding to the highest GRG reported in Table 7 (Exp. 5). This approach is consistent with prior optimization studies and ensures a fair comparison between an experimentally observed optimum and a statistically derived factor-level optimum [32,

Table 9. ANOVA for printing time, part weight, compressive strength, and GRG.

Response	Source	DOF	Adj SS	Adj MS	*F*-value	*p*-value	% contribution
Printing Time (min)	Layer height (mm)	1	134.295	134.295	724.33	0.001	84.82
	Wall thickness (mm)	1	0.007	0.007	0.04	0.848	0.00
	Infill density (%)	1	18.679	18.679	100.74	0.001	11.80
	Nozzle temperature (°C)	1	0.014	0.014	0.08	0.786	0.01
	Bed temperature (°C)	1	0.025	0.025	0.13	0.719	0.02
	Printing speed (mm/s)	1	1.979	1.979	10.67	0.004	1.25
	Error	18	3.337	0.185			2.11
	Total	24	158.336				100
Part Weight (g)	Layer height (mm)	1	0.4918	0.4918	2.61	0.123	1.88
	Wall thickness (mm)	1	2.1275	2.1275	11.30	0.003	8.14
	Infill density (%)	1	20.0309	20.0309	106.40	0.001	76.67
	Nozzle temperature (°C)	1	0.0128	0.0128	0.07	0.797	0.05
	Bed temperature (°C)	1	0.0320	0.0320	0.17	0.685	0.12
	Printing speed (mm/s)	1	0.0418	0.0418	0.22	0.643	0.16
	Error	18	3.3887	0.1883			12.97
	Total	24	26.1256				100
Compressive Strength (MPa)	Layer height (mm)	1	0.000	0.000	0.00	0.999	0.00
	Wall thickness (mm)	1	11.738	11.738	4.53	0.047	4.25
	Infill density (%)	1	213.817	213.817	82.47	0.001	77.33
	Nozzle temperature (°C)	1	3.616	3.616	1.39	0.253	1.31
	Bed temperature (°C)	1	0.647	0.647	0.25	0.623	0.23
	Printing speed (mm/s)	1	0.003	0.003	0.00	0.974	0.00
	Error	18	46.670	2.593			16.88
	Total	24	276.490				100
GRG	Layer height (mm)	1	0.09625	0.09625	57.52	0.001	20.00
	Wall thickness (mm)	1	0.00748	0.00748	4.47	0.049	1.55
	Infill density (%)	1	0.34504	0.34504	206.21	0.001	71.69
	Nozzle temperature (°C)	1	0.00002	0.00002	0.01	0.914	0.00
	Bed temperature (°C)	1	0.00127	0.00127	0.76	0.395	0.26
	Printing speed (mm/s)	1	0.00110	0.00110	0.66	0.428	0.23
	Error	18	0.03012	0.00167			6.26
	Total	24	0.48128				100

42].

The baseline condition (Exp. 5) corresponds to the parameter combination LH1–WT5–ID5–NT5–BT5–PS5, whereas the optimized setting derived from the GRG level-means analysis (Table 8) is LH1–WT3–ID5–NT4–BT3–PS2, corresponding to a layer height of 0.06 mm, wall thickness of 0.6 mm, infill density of 100%, nozzle temperature of 210 °C, bed temperature of 50 °C, and printing speed of 30 mm/s. Three specimens were fabricated using the optimized setting. Table 10 summarizes the average printing time (P_T), part weight (P_W), compressive strength (C_S), and GRG obtained for both the baseline and optimized conditions, along with the corresponding percentage changes.

Relative to the baseline, the optimized setting reduced P_T from 66.00 min to 64.50 min (−2.27%) and P_W from 0.577 g to 0.554 g (−3.99%). Simultaneously, C_S increased substantially from 35.919 MPa to 44.396 MPa, representing an improvement of 23.6%. Consequently, the composite GRG increased from 0.8572 to 0.8839 (+3.11%). These outcomes confirm that the factor-level optimum identified by the TM–GRA–PCA approach yields a superior multi-objective compromise relative to the best experimental trial in the orthogonal array. The improvement is mainly reflected in C_S, while P_T and P_W remained slightly lower than the baseline, indicating that the optimized condition improved mechanical screening performance without sacrificing manufacturing efficiency.

From a mechanistic perspective, the improvement in compressive strength is primarily attributed to enhanced interlayer bonding quality and load-transfer efficiency under the selected thermal and deposition conditions, while maintaining a high effective cross-sectional area via 100% infill. The concurrent reductions in printing time and part weight are consistent with the reduced wall thickness, which lowers shell material volume and offsets the influence of the slightly reduced printing speed. Using 100% infill maintained internal load-path continuity, whereas reducing the wall thickness from 1.0 mm to 0.6 mm reduced shell mate-

Table 10. Results of the confirmation test.

Setting	P_T (min)	P_W (g)	C_s (MPa)	GRG	Improvement (%)			
					P_T	P_W	C_S	GRG
Initial/baseline condition: $LH_1WT_5ID_5NT_5BT_5PS_5$	66.00	0.577	35.919	0.8572				
Optimized: $LH_1WT_3ID_5NT_4BT_3PS_2$	64.50	0.554	44.396	0.8839	-2.27	-3.99	+23.6	+3.11

rial consumption without eliminating the wall's contribution to the stress distribution in the threaded geometry.

For additional benchmarking, the compressive strength of the PLA+ bone screw-like specimens in this study can be compared with values reported in the literature for similar 3D-printed PLA screws. In a study by Dhandapani et al. [6], the maximum compressive strength of solid (100% infill) PLA cortical screws was 26.13 ± 0.56 MPa. By comparison, the PLA+ screw-like specimens fabricated with our optimized parameters reached ~ 44.4 MPa. This represents a clear improvement in mechanical performance, highlighting the combined benefits of the modified PLA+ material and the optimized FDM process settings. However, this comparison is limited to compressive screening performance and does not establish equivalence to clinically used cortical bone screws. ASTM F543 emphasizes screw-specific mechanical behavior, and direct clinical acceptability cannot be inferred from compressive strength alone.

Although the optimized C_S value is higher than the cited value for 3D-printed PLA cortical screws, clinical suitability requires additional evidence. In particular, torsional strength, insertion and removal torque, pull-out resistance, and fatigue durability should be evaluated before the printed PLA+ screw-like specimens are considered for orthopedic fixation applications. Therefore, the present confirmation test validates the manufacturing-oriented optimization result, not full implant qualification.

As an additional verification, we predicted the expected GRG at the optimal setting and compared it with the experimentally measured value. The Taguchi predictive formula for the expected performance [50, 51] was calculated by:

$$\gamma_{predicted} = \gamma_m + \sum_{i=1}^{q} \gamma_0 - \gamma_m \tag{10}$$

where γ_0 denotes the highest mean GRG at the selected levels, γ_m is the overall mean GRG, and q is the number of parameters.

The agreement between the predicted and experimental GRG values from the confirmation tests was evaluated using a confidence interval (CI) [50–52] defined by:

$$CI = \sqrt{F_\alpha\,(1, f_e) \times V_e \times \left[\frac{1}{n_{eff}} + \frac{1}{R}\right]} \tag{11}$$

where $F_\alpha\,(1, f_e) = F$ ratio required for α; $\alpha =$ risk; $f_e =$ DoF of error; $V_e =$ variance of error; $n_{eff} =$ effective number of replications.

Finally, the predicted GRG for the optimized setting was calculated using Eq. (10) as 0.9830. The agreement between predicted and experimental GRG values was assessed using the confidence interval (CI) defined by Eq. (11), yielding a 95% confidence interval of $0.6976 < \gamma_{experimental} < 1.2684$. The experimentally obtained GRG of 0.8839 lies within this interval, confirming the reliability of the confirmation test and further validating the effectiveness of the TM–GRA–PCA framework in identifying manufacturing-oriented optimal parameter combinations.

Overall, the confirmation experiment supports the effectiveness of the integrated TM–GRA–PCA framework in identifying a manufacturing-oriented compromise setting. The optimized parameters substantially increased compressive strength while maintaining printing time and part weight comparable to the best trial in the original orthogonal array.

The generalizability of the numerical optimum should be treated with caution. The specific values—such as a 0.06 mm layer height, 0.6 mm wall thickness, 100% infill, 210 °C nozzle temperature, 50 °C bed temperature, and 30 mm/s printing speed—are tailored to the Creality Ender-6 platform, eSUN PLA+ filament, a 0.2 mm nozzle, Cura 5.5.0 for toolpath generation, and the particular auxiliary settings used here. The key takeaway is the parameter hierarchy and the process window, informed by mechanisms rather than by a universal set of settings. Other FDM systems should adjust nozzle and bed temperatures, flow rate, cooling, extrusion width, and speed limits accordingly, and conduct a smaller calibration test specific to their printer, filament, and nozzle before adopting these settings.

4. Conclusions

This study optimized the fused deposition modeling (FDM) process parameters for manufacturing PLA+ bone screw-like specimens using an integrated multi-response framework combining the Taguchi method, grey relational analysis (GRA), and principal component analysis (PCA). The main novelty lies in the combined treatment of PLA+ material, bone screw-like geometry, three competing responses, and PCA-derived objective weighting within a single experimentally confirmed optimization framework. The factor-level optimum derived from the grey relational grade (GRG) level-mean analysis corresponds to a layer height of 0.06 mm, wall thickness of 0.6 mm, infill density of 100%, nozzle temperature of 210 °C, bed temperature of 50 °C, and printing speed of 30 mm/s. Relative to the best-performing trial in the original L25 orthogonal array, confirmation testing demonstrated an increase in the overall GRG from 0.8572 to 0.8839 (+3.11%), accompanied by improved compressive strength (≈ 44.4 MPa) and modest reductions in printing time (≈ 64.5 min) and part weight (≈ 0.554 g).

Analysis of variance on the composite GRG confirmed that infill density is the dominant contributor to multi-objective performance, accounting for approximately 71.69% of the observed variance, followed by layer height (≈ 20.00%) and wall thickness (≈ 1.55%) within the investigated parameter ranges. These results are consistent with the underlying process mechanics: infill density and wall thickness primarily control the effective load-bearing cross-section and internal porosity, thereby governing compressive strength while also influencing part weight and printing time, whereas layer height dictates layer count and toolpath length, strongly affecting printing time and bonding-related morphology. Mechanistically, higher infill density improves internal load-path continuity, wall thickness modifies shell-supported stress distribution in the threaded region, and layer height influences interlayer bonding and potential interfacial failure paths.

Beyond identifying an improved parameter combination, this study demonstrates the utility of PCA-derived weighting for aggregating multiple competing objectives into a single data-driven performance index. When reported alongside the equal-weight GRA, the weighted GRG provides transparency into the relative importance of individual responses and the robustness of the identified optimum to weighting assumptions.

This study was intentionally framed as a manufacturing process optimization effort, using compressive strength as a screening metric together with productivity- and material-related measures. Compression alone is insufficient to qualify orthopedic fixation screws. Therefore, the optimized compressive strength of approximately 44.4 MPa should not be interpreted as direct evidence of clinical acceptability or equivalence to cortical bone screw requirements. ASTM F543-related qualification requires screw-specific mechanical evaluation beyond axial compression. Future work should therefore include torsional, pull-out, and fatigue testing; direct failure-mode analysis using post-test imaging or fractography; assessment of sterilization and environmental degradation effects; microstructural characterization of porosity and interlayer bonding; and validation across different printers, nozzle diameters, slicer versions, and filament batches. Overall, the experimentally supported TM–GRA–PCA pipeline provides a reproducible approach for balancing competing objectives in PLA+ FDM printing of bone screw-like geometries while clearly delineating the steps required for functional and clinical qualification of the printed parts.

More specifically, future ASTM F543-aligned validation should include torsional testing, insertion/removal torque measurement, axial pull-out resistance evaluation, and cyclic fatigue testing before any fixation-relevant claims are made.

References

[1] M. Bardot and M. D. Schulz, (2020) *"Biodegradable poly(lactic acid) nanocomposites for fused deposition modeling 3D printing"* **Nanomaterials *10***: 2567. DOI: 10.3390/nano10122567.

[2] S. Sharma, D. Mudgal, and V. Gupta, (2024) *"Integrating extrusion process and additive manufacturing for biomedical breakthroughs"* **International Journal on Interactive Design and Manufacturing (IJIDeM) *18***: 3547–3570. DOI: 10.1007/s12008-023-01632-x.

[3] R. Agarwal, V. Gupta, and J. Singh, (2022) *"Additive manufacturing-based design approaches and challenges for orthopaedic bone screws: a state-of-the-art review"* **Journal of the Brazilian Society of Mechanical Sciences and Engineering *44***: 37. DOI: 10.1007/s40430-021-03331-8.

[4] A. Grivet-Brancot, M. Boffito, and G. Ciardelli, (2022) *"Use of Polyesters in Fused Deposition Modeling for Biomedical Applications"* **Macromolecular Bioscience *22***: 2200039. DOI: 10.1002/mabi.202200039.

[5] R. Agarwal, V. Gupta, and J. Singh, (2022) *"Mechanical and biological behaviour of additive manufactured biomimetic biodegradable orthopaedic cortical screws"* **Rapid Prototyping Journal *28***: 1690–1705. DOI: 10.1108/RPJ-01-2022-0006.

[6] R. Dhandapani, P. D. Krishnan, A. Zennifer, V. Kannan, A. Manigandan, M. R. Arul, D. Jaiswal, A. Subramanian, S. G. Kumbar, and S. Sethuraman, (2020) *"Additive manufacturing of biodegradable porous orthopaedic screw"* **Bioactive Materials *5***: 458–467. DOI: 10.1016/j.bioactmat.2020.03.009.

[7] A. Joseph and V. Uthirapathy, (2024) *"A Systematic Review of the Contribution of Additive Manufacturing toward Orthopedic Applications"* **ACS Omega *9***: 44042–44075. DOI: 10.1021/acsomega.4c04870.

[8] Y. Karayer, Ş. Altınsoy, G. Koç, D. Can, and Y. E. Toğar, (2025) *"Effects of Steam Sterilization and Recycling on the Mechanical and Surface Properties of 3D-Printed Biodegradable PLA and Re-PLA Materials"* **Polymers *17***: 2590. DOI: 10.3390/polym17192590.

[9] E. Kargar and A. Ghasemi-Ghalebahman, (2023) *"Experimental investigation on fatigue life and tensile strength of carbon fiber-reinforced PLA composites based on fused deposition modeling"* **Scientific Reports *13***: 18194. DOI: 10.1038/s41598-023-45046-x.

[10] V. C. Agbakoba, P. Hlangothi, J. Andrew, and M. J. John, (2022) *"Mechanical and Shape Memory Properties of 3D-Printed Cellulose Nanocrystal (CNC)-Reinforced Polylactic Acid Bionanocomposites for Potential 4D Applications"* **Sustainability *14***: 12759. DOI: 10.3390/su141912759.

[11] E. Hozdić and R. Hasanagić, (2024) *"Analysis of the Impact of Cooling Lubricants on the Tensile Properties of FDM 3D Printed PLA and PLA+CF Materials"* **Polymers *16***: 2228. DOI: 10.3390/polym16152228.

[12] V. DeStefano, S. Khan, and A. Tabada, (2020) *"Applications of PLA in modern medicine"* **Engineered Regeneration *1***: 76–87. DOI: 10.1016/j.engreg.2020.08.002.

[13] J.-W. Li, C.-F. Du, C.-X. Yuchi, and C.-Q. Zhang, (2019) *"Application of Biodegradable Materials in Orthopedics"* **Journal of Medical and Biological Engineering *39***: 633–645. DOI: 10.1007/s40846-019-00469-8.

[14] H. Zhou, Z. Song, and S. Cai, (2020) *"Toughening of poly(lactide acid) with low crystallinity through biaxial poststretching"* **Journal of Polymer Science *58***: 3488–3495. DOI: 10.1002/pol.20200526.

[15] L. Sandanamsamy, W. S. W. Harun, I. Ishak, F. R. M. Romlay, K. Kadirgama, D. Ramasamy, S. R. A. Idris, and F. Tsumori, (2023) *"A comprehensive review on fused deposition modelling of polylactic acid"* **Progress in Additive Manufacturing *8***: 775–799. DOI: 10.1007/s40964-022-00356-w.

[16] T. M. Joseph, A. Kallingal, A. M. Suresh, D. K. Mahapatra, M. S. Hasanin, J. Haponiuk, and S. Thomas, (2023) *"3D printing of polylactic acid: recent advances and opportunities"* **The International Journal of Advanced Manufacturing Technology *125***(3): 1015–1035. DOI: https://doi.org/10.1007/s00170-022-10795-y.

[17] R. Agarwal, J. Singh, and V. Gupta, (2025) *"A data-driven ensemble machine learning approach for predicting the mechanical strength of 3D printed orthopaedic bone screws"* **Proceedings of the Institution of Mechanical Engineers, Part E: Journal of Process Mechanical Engineering *239***: 1650–1662. DOI: 10.1177/09544089231211235.

[18] M. M. Rahman, J. Sultana, S. B. Rayhan, and A. Ahmed, (2023) *"Optimization of FDM manufacturing parameters for the compressive behavior of cubic lattice cores: an experimental approach by Taguchi method"* **The International Journal of Advanced Manufacturing Technology *129***: 1329–1343. DOI: 10.1007/s00170-023-12342-9.

[19] U. K. uz Zaman, E. Boesch, A. Siadat, M. Rivette, and A. A. Baqai, (2019) *"Impact of fused deposition modeling (FDM) process parameters on strength of built parts using Taguchi's design of experiments"* **The International Journal of Advanced Manufacturing Technology *101***: 1215–1226. DOI: 10.1007/s00170-018-3014-6.

[20] A. Elkaseer, S. Schneider, and S. G. Scholz, (2020) *"Experiment-Based Process Modeling and Optimization for High-Quality and Resource-Efficient FFF 3D Printing"* **Applied Sciences *10***: 2899. DOI: 10.3390/app10082899.

[21] E. U. Enemuoh, S. Duginski, C. Feyen, and V. G. Menta, (2021) *"Effect of Process Parameters on Energy Consumption, Physical, and Mechanical Properties of Fused Deposition Modeling"* **Polymers *13***: 2406. DOI: 10.3390/polym13152406.

[22] B. A. Ahmed, U. Nadeem, A. S. Hakeem, A. Ul-Hamid, M. Y. Khan, M. Younas, and H. A. Saeed, (2023) *"Printing Parameter Optimization of Additive Manufactured PLA Using Taguchi Design of Experiment"* **Polymers *15***: 4370. DOI: 10.3390/polym15224370.

[23] A. Hasan, M. Fahad, and M. A. Khan, (2024) *"Effect of print parameters on the tensile strength and built time of FDM-printed PLA parts"* **The International Journal of Advanced Manufacturing Technology *132***: 3047–3065. DOI: 10.1007/s00170-024-13506-x.

[24] J. D. Kechagias, (2024) *"3D printing parametric optimization using the power of Taguchi design: an expository paradigm"* **Materials and Manufacturing Processes *39***: 797–803. DOI: 10.1080/10426914.2023.2290258.

[25] C. Camposeco-Negrete, J. Varela-Soriano, and J. J. Rojas-Carreón, (2021) *"The effects of printing parameters on quality, strength, mass, and processing time of polylactic acid specimens produced by additive manufacturing"* **Progress in Additive Manufacturing *6***: 821–840. DOI: 10.1007/s40964-021-00198-y.

[26] S. Pachauri, N. K. Gupta, and A. Gupta, (2025) *"Influence of 3D printing process parameters on the mechanical properties of polylactic acid (PLA) printed with fused filament fabrication: experimental and statistical analysis"* **International Journal on Interactive Design and Manufacturing (IJIDeM) *19***: 1159–1177. DOI: 10.1007/s12008-023-01424-3.

[27] A. Alafaghani and A. Qattawi, (2018) *"Investigating the effect of fused deposition modeling processing parameters using Taguchi design of experiment method"* **Journal of Manufacturing Processes *36***: 164–174. DOI: 10.1016/j.jmapro.2018.09.025.

[28] J. Sultana, M. M. Rahman, Y. Wang, A. Ahmed, and C. Xiaohu, (2024) *"Influences of 3D printing parameters on the mechanical properties of wood PLA filament: an experimental analysis by Taguchi method"* **Progress in Additive Manufacturing *9***: 1239–1251. DOI: 10.1007/s40964-023-00516-6.

[29] G. Nyiranzeyimana, J. Mutua, B. Mose, and T. Mbuya, (2022) *"A grey-based Taguchi method to optimize fused deposition modelling process parameters for manufacture of a hip joint implant"* **Materialwissenschaft und Werkstofftechnik *53***: 89–108. DOI: 10.1002/mawe.202100129.

[30] A. H. Kadhum, S. Al-Zubaidi, and S. S. A. AlKareem, (2023) *"Optimization of Mechanical Properties and Surface Characteristics of PLA+ 3D Printing Materials"* **International Journal of Chemical Engineering *2023***: 1–15. DOI: 10.1155/2023/8887905.

[31] R. Ranjan and A. Saha, (2024) *"A novel hybrid multi-criteria optimization of 3D printing process using grey relational analysis (GRA) coupled with principal component analysis (PCA)"* **Engineering Research Express *6***: 015080. DOI: 10.1088/2631-8695/ad2320.

[32] R. Agarwal, H. K. Mehtani, J. Singh, and V. Gupta, (2022) *"Post-yielding fracture mechanics of 3D printed polymer-based orthopedic cortical screws"* **Polymer Composites *43***: 6829–6837. DOI: 10.1002/pc.26620.

[33] Y. Kuo, T. Yang, and G.-W. Huang, (2008) *"The use of grey relational analysis in solving multiple attribute decision-making problems"* **Computers & Industrial Engineering *55***: 80–93. DOI: 10.1016/j.cie.2007.12.002.

[34] ASTM. *ASTM F543-23: Specification and Test Methods for Metallic Medical Bone Screws*. 2023. DOI: 10.1520/F0543-23.

[35] J. Singh, K. K. Goyal, R. Kumar, and V. Gupta, (2022) *"Influence of process parameters on mechanical strength, build time, and material consumption of 3D printed polylactic acid parts"* **Polymer Composites *43***: 5908–5928. DOI: 10.1002/pc.26849.

[36] M. Fahad, M. Mujeeb, and M. A. Khan, (2023) *"Effect of Process Parameters on the Compressive and Impact Strength of 3D Printed Parts"* **Iranian Journal of Science and Technology, Transactions of Mechanical Engineering *47***: 257–265. DOI: 10.1007/s40997-022-00514-z.

[37] J. D. Kechagias, N. Vidakis, M. Petousis, and N. Mountakis, (2023) *"A multi-parametric process evaluation of the mechanical response of PLA in FFF 3D printing"* **Materials and Manufacturing Processes *38***: 941–953. DOI: 10.1080/10426914.2022.2089895.

[38] L. Auffray, P.-A. Gouge, and L. Hattali, (2022) *"Design of experiment analysis on tensile properties of PLA samples produced by fused filament fabrication"* **The International Journal of Advanced Manufacturing Technology *118***: 4123–4137. DOI: 10.1007/s00170-021-08216-7.

[39] V. Darji, S. Singh, and H. S. Mali, (2023) *"Mechanical characterization of additively manufactured polymer composites: A state-of-the-art review and future scope"* **Polymer Composites *44***: 4370–4419. DOI: 10.1002/pc.27431.

[40] S. Chakraborty, H. N. Datta, and S. Chakraborty, (2023) *"Grey Relational Analysis-Based Optimization of Machining Processes: a Comprehensive Review"* **Process Integration and Optimization for Sustainability *7***: 609–639. DOI: 10.1007/s41660-023-00311-4.

[41] Y. Kuo, T. Yang, and G.-W. Huang, (2008) *"The use of a grey-based Taguchi method for optimizing multi-response simulation problems"* **Engineering Optimization *40***: 517–528. DOI: 10.1080/03052150701857645.

[42] O. Tunçel, K. Tüfekci, and Ç. Kahya, (2024) *"Multi-objective optimization of 3D printing process parameters using gray-based Taguchi for composite PLA parts"* **Polymer Composites *45***: 12870–12884. DOI: 10.1002/pc.28674.

[43] A. Bademlioglu, A. Canbolat, and O. Kaynakli, (2020) *"Multi-objective optimization of parameters affecting Organic Rankine Cycle performance characteristics with Taguchi-Grey Relational Analysis"* **Renewable and Sustainable Energy Reviews *117***: 109483. DOI: 10.1016/j.rser.2019.109483.

[44] C.-F. J. Kuo, T.-L. Su, P.-R. Jhang, C.-Y. Huang, and C.-H. Chiu, (2011) *"Using the Taguchi method and grey relational analysis to optimize the flat-plate collector process with multiple quality characteristics in solar energy collector manufacturing"* **Energy *36***: 3554–3562. DOI: 10.1016/j.energy.2011.03.065.

[45] S. B. Sutono, S. H. A. Rashid, Z. Taha, N. Subagyo, and H. Aoyama, (2017) *"Integration of grey-based Taguchi method and principal component analysis for multi-response decision-making in Kansei engineering"* **European Journal of Industrial Engineering *11***: 205–227. DOI: 10.1504/EJIE.2017.083254.

[46] Z. A. Khan, S. Kamaruddin, and A. N. Siddiquee, (2010) *"Feasibility study of use of recycled High Density Polyethylene and multi response optimization of injection moulding parameters using combined grey relational and principal component analyses"* **Materials & Design *31***: 2925–2931. DOI: 10.1016/j.matdes.2009.12.028.

[47] I. T. Jolliffe. *Principal Component Analysis*. New York: Springer-Verlag, 2002. DOI: 10.1007/b98835.

[48] G. Gao, F. Xu, J. Xu, G. Tang, and Z. Liu, (2022) *"A Survey of the Influence of Process Parameters on Mechanical Properties of Fused Deposition Modeling Parts"* **Micromachines *13***: 553. DOI: 10.3390/mi13040553.

[49] M. A. Mazlan, M. A. Anas, N. A. N. Izmin, and A. H. Abdullah, (2023) *"Effects of Infill Density, Wall Perimeter and Layer Height in Fabricating 3D Printing Products"* **Materials *16***: 695. DOI: 10.3390/ma16020695.

[50] J. K. Abifarin, (2021) *"Taguchi grey relational analysis on the mechanical properties of natural hydroxyapatite: effect of sintering parameters"* **The International Journal of Advanced Manufacturing Technology *117***: 49–57. DOI: 10.1007/s00170-021-07288-9.

[51] J. K. Abifarin, M. U. Suleiman, E. A. Abifarin, F. B. Fidelis, O. K. Oyelakin, D. I. Jacob, and M. Y. Abdulrahim, (2022) *"Fabrication of mechanically enhanced hydroxyapatite scaffold with the assistance of numerical analysis"* **The International Journal of Advanced Manufacturing Technology *118***: 3331–3344. DOI: 10.1007/s00170-021-08184-y.

[52] O. A. Osuchukwu, A. Salihi, I. Abdullahi, and D. O. Obada, (2022) *"Taguchi grey relational optimization of sol–gel derived hydroxyapatite from a novel mix of two natural biowastes for biomedical applications"* **Scientific Reports *12***: 17968. DOI: 10.1038/s41598-022-22888-5.